arXiv:1611.05192v1 [astro-ph.CO] 16 Nov 2016

Projected Axis Ratios of Galaxy Clusters in the Horizon-AGN Simulation: Impact of Baryon Physics and Comparison with Observations

Daichi SUTO [1], Sébastien PEIRANI [2,3], Yohan DUBOIS [2], Tetsu KITAYAMA [4], Takahiro NISHIMICHI [3,5], Shin SASAKI [6], and Yasushi SUTO [1,7]

[1]Department of Physics, The University of Tokyo, Tokyo 113-0033, Japan

[2]CNRS and UPMC Université Paris 06, UMR 7095, Institut d'Astrophysique de Paris, 98 bis Boulevard Arago, Paris 75014, France

[3]Kavli Institute for the Physics and Mathematics of the Universe (WPI), The University of Tokyo Institutes for Advanced Study, The University of Tokyo, 5-1-5 Kashiwanoha, Kashiwa 277-8583, Japan

[4]Department of Physics, Toho University, Funabashi, Chiba 274-8510, Japan

[5]CREST, JST, 4-1-8 Honcho, Kawaguchi, Saitama, 332-0012, Japan

[6]Department of Physics, Tokyo Metropolitan University, Hachioji, Tokyo 192-0397, Japan

[7]Research Center for the Early Universe, School of Science, The University of Tokyo, Tokyo 113-0033, Japan

*E-mail: suto@phys.s.u-tokyo.ac.jp

Received ; Accepted

Abstract

We characterize the non-sphericity of galaxy clusters by the projected axis ratio of spatial distribution of star, dark matter, and X-ray surface brightness (XSB). We select 40 simulated groups and clusters of galaxies with mass larger than $5 \times 10^{13} M_\odot$ from the Horizon simulation that fully incorporates the relevant baryon physics, in particular, the AGN feedback. We find that the baryonic physics around the central region of galaxy clusters significantly affects the non-sphericity of dark matter distribution even beyond the central region, approximately up to the half of the virial radius. Therefore it is very difficult to predict the the probability density

function (PDF) of the projected axis ratio of XSB from dark-matter only N-body simulations as attempted in previous studies. Indeed we find that the PDF derived from our simulated clusters exhibits much better agreement with that from the observed X-ray clusters. This indicates that our present methodology to estimate the non-sphericity directly from the Horizon simulation is useful and promising. Further improvements in both numerical modeling and observational data will establish the non-sphericity of clusters as a cosmological test complementary to more conventional statistics based on spherically averaged quantities.

Key words: Cosmology: dark matter; large-scale structure of Universe; Galaxies: clusters: general

1 Introduction

Statistics of galaxy clusters, along with cosmic microwave background and large-scale distribution of galaxies, has made significant contribution to the establishment of the standard cosmological model dominated by cold dark matter (CDM). Indeed the resulting CDM paradigm has passed a variety of theoretical and observational tests, except for somewhat controversial problems on small scales. While there are a number of important successes in terms of the spherically averaged properties (e.g., Press & Schechter 1974; Navarro et al. 1996, 1997; Suto et al. 2016a), observed galaxy clusters are typically far from spherical. Nevertheless a majority of previous studies on galaxy clusters has not properly taken into account their non-sphericity.

In the previous paper (Suto et al. 2016b), we found that the evolution of non-sphericity in N-body simulations is not in quantitative agreement with a simple model of ellipsoidal collapse. We also found that the probability density function (PDF) of projected axis ratios of dark matter halos is empirically well approximated by the beta function, which is fairly insensitive to the mass and redshift of those halos. While the latter result is potentially useful in confronting the result with the data of weak lensing halos, there are a couple of fundamental limitations. One is that the currently available number of good-quality weak-lensing data is quite limited. The other is that the axis ratio from the lensing shear map needs to be measured without assuming the self-similarity in the non-sphericity of halos (see, *e.g.*, Oguri et al. 2010; Suto et al. 2016b).

Therefore we consider, instead, the non-sphericity of the X-ray surface brightness (XSB) S_X of galaxy clusters in the present paper. Since S_X is one of the primary observables for galaxy clusters, a large number of high-quality data-sets are already available, and also is expected to further increase in the near future. In fact, Kawahara (2010) has measured the non-sphericity of the XSB of 61 galaxy

clusters, and reported that the PDF of their axis ratio is consistent with the prediction on the basis of Jing & Suto (2002) and Oguri et al. (2003).

We will revisit the problem in the present paper because the theoretical prediction of non-sphericity of S_X is more difficult than the observational measurements due to the complicated effects of baryons in galaxy clusters (Debattista et al. 2008; Teyssier et al. 2011; Bryan et al. 2013; Butsky et al. 2015; Cui et al. 2016).

The distribution of gas is generally different from that of dark matter in clusters (Lee & Suto 2003). Under the assumption of hydrostatic equilibrium (HSE), the gas mass density $\rho_{\rm gas}$ satisfies the following equation:

$$\frac{1}{\rho_{\rm gas}}\nabla p = -\nabla\phi, \tag{1}$$

where p is the gas pressure, and ϕ is the gravitational potential mainly determined by the dark matter density distribution. If the gas is isothermal, Equation (1) reduces to $\nabla \log \rho_{\rm gas} \propto \nabla\phi$. Thus the resulting gas distribution traces the *isopotential* surface, instead of the *isodensity* surface of the underlying dark matter. Since the isopotential surfaces tend to be rounder than the isodensity surfaces, gas distribution becomes more spherical than that of dark matter (Lee & Suto 2003).

In reality, the conventional assumption of HSE is not so accurate (Lau et al. 2009, 2013; Fang et al. 2009; Suto et al. 2013) due to the dynamical motion of gas. For those reasons, the non-sphericity of gas distribution cannot be related to that of dark matter distribution in a straightforward fashion. Hence it is essential to use numerical simulations including gas physics in order to precisely study the non-sphericity of gas density, and therefore that of S_X of galaxy clusters. This is exactly what we will address in this paper.

The rest of the paper is organized as follows. Section 2 briefly describes the Horizon simulation that we use in modeling the non-sphericity of galaxy clusters. We emphasize the important role of baryon physics, in particular, the active galactic nuclei (AGNs) feedback by considering spherically-averaged density and temperature profiles. Then we measure the axis ratios of dark matter, stellar, and XSB distributions for simulated galaxy clusters in Section 3. Section 4 compares the PDF of the axis ratios constructed from 40 simulated clusters against that computed by Kawahara (2010) for observed 61 clusters. Final section is devoted to summary and discussion.

2 Numerical Modeling

2.1 Horizon simulation

Our current study is entirely based on samples of simulated groups and clusters of galaxies extracted from three cosmological hydrodynamical runs, Horizon-AGN ($\rm H_{AGN}$), Horizon-noAGN ($\rm H_{noAGN}$),

and Horizon-DM ($\mathrm{H_{DM}}$). Results of $\mathrm{H_{AGN}}$ are already described in detail in Dubois et al. (2014), so we briefly describe here the major feature of those runs that is relevant to our current discussion.

The simulation adopts a set of cosmological parameters derived from the Wilkinson Microwave Anisotropy Probe 7 year (Komatsu et al. 2011); $\Omega_{m,0} = 0.272$, $\Omega_{\Lambda,0} = 0.728$, $\Omega_{b,0} = 0.045$, $\sigma_8 = 0.81$, $H_0 = 70.4$ km s^{-1} Mpc^{-1}, and $n_s = 0.967$. The simulation runs employ 1024^3 dark matter particles in a periodic cube with a side length of 100 h^{-1} Mpc, which results in a dark matter mass resolution of $8.27 \times 10^7 M_\odot$. The three runs adopt the identical initial conditions that are generated with the `MPGRAFIC` software (Prunet et al. 2008), except the fact that the dark matter density parameter in $\mathrm{H_{DM}}$ is set as $\Omega_{m,0}$, instead of $\Omega_{m,0} - \Omega_{b,0}$ in $\mathrm{H_{AGN}}$ and $\mathrm{H_{noAGN}}$.

Hydrodynamics of gas and other baryon physics is solved on grids over the simulation box. The size of gas cells is initially set to 136 kpc, and is refined subsequently when the number of dark matter particles in a cell becomes more than eight, or when the total baryonic mass in a cell becomes eight times the dark matter mass resolution ($8.27 \times 10^7 M_\odot$). The refinement is carried out up to 7 times, and therefore the minimum cell size is 1.06 kpc.

The radiative cooling of gas due to H, He, and metals is modeled according to Sutherland & Dopita (1993). Heating from a uniform UV background is also implemented following Haardt & Madau (1996). Star particles are created according to the Schmidt-Kennicutt law using a random Poisson process (Rasera & Teyssier 2006; Dubois & Teyssier 2008) if the gas hydrogen number density in a cell exceeds the threshold of $n_0 = 0.1$ cm^{-3}. In addition, feedback from stellar winds, supernovae (SNe) type Ia and II are also taken into account for mas, energy, and metal release.

Type II SNe are taken into account assuming the Salpeter initial mass function. The SN energy is released into the surrounding gas according to the Sedov blast wave solution because the thermal input is radiated away due to the efficient gas cooling in high-density regions. The frequency of Type Ia SN explosions follows Greggio & Renzini (1983), and the mechanical energy from Type II SNe is taken from `STARBURST99` (Leitherer et al. 1999, 2010).

It is known that the feedback from AGNs plays a significant role in the evolution of a central part of galaxy clusters. The AGN feedback in the present simulations is incorporated following Dubois et al. (2012). Black holes (BHs) of an initial seed mass $10^5 M_\odot$ are created when the gas mass density $\rho_{\rm gas}$ in a cell exceeds $m_{\rm H} n_0$, with $m_{\rm H}$ being the hydrogen mass. Since the accretion onto BHs cannot be resolved in the current simulations, their growth is empirically computed adopting the Bondi-Hoyle-Lyttleton accretion rate $\dot{M}_{\rm BH}$. Depending on the ratio $\chi \equiv \dot{M}_{\rm BH}/\dot{M}_{\rm Edd}$ relative to the Eddington rate, the AGN feedback is divided into two different modes. In the radio mode ($\chi < 0.01$), the feedback energy is ejected into a bipolar outflow with a jet velocity of 10^4 km s^{-1} following Omma et al. (2004). Otherwise, the feedback is in the quasar mode ($\chi > 0.01$) in which thermal energy is

isotropically injected into gas.

The first simulation, $\mathrm{H_{AGN}}$, is a full hydrodynamic run with gas cooling and both SN and AGN feedback. The second one, $\mathrm{H_{noAGN}}$, is a hydrodynamic simulation with gas cooling and SN feedback, but without AGN feedback. Finally $\mathrm{H_{DM}}$ is a dark matter only run without baryon physics. The first is our main simulation, and the other two are used for reference to examine the effect of AGN feedback and baryon physics. The three runs ($\mathrm{H_{AGN}}$, $\mathrm{H_{noAGN}}$, and $\mathrm{H_{DM}}$) are performed using the the same initial conditions and sub-grid modeling.

We extract all 40 halos with mass larger than $5 \times 10^{13} M_{\odot}$ from $\mathrm{H_{AGN}}$ using the AdaptaHOP halofinder (Aubert et al. 2004). Since those halos are not spherical, we decided to characterize them in terms of M_{200}, the mass of a sphere within which the mean density is 200 times the cosmic critical density at $z = 0$. In most cases, the resulting value of M_{200} is close to that defined by the AdaptaHOP halofinder, but in some cases is smaller because of the presence of substructures.

In reality, the mass scale of the halos corresponds to that of groups and clusters of galaxies, but we simply call them clusters in what follows. The counterparts of the clusters in three different runs are identified as follows. Since we start from the same initial conditions, each dark matter particle shares a common identity between the 3 simulations. If more than 75% of the member particles of a given halo from $\mathrm{H_{AGN}}$ are found in another halo from $\mathrm{H_{noAGN}}$ and $\mathrm{H_{DM}}$ runs, then we assume that these redobjects are the counterparts of $\mathrm{H_{AGN}}$ run. Indeed, we can find the counterparts for all the 40 clusters with this procedure.

In the following sections, we analyze the non-sphericity of XSB for the two sets of 40 clusters in $\mathrm{H_{AGN}}$ and $\mathrm{H_{noAGN}}$. For comparison, we also discuss the non-sphericity of dark matter halos for the three sets of 40 clusters.

Of course, no simulation is perfect, and $\mathrm{H_{AGN}}$ should be rather regarded as one of the most successful simulation runs. As we will show below, the non-sphericity of galaxy clusters is very sensitive to the baryon physics, and we have to keep in mind that $\mathrm{H_{AGN}}$ is nothing more than an empirically calibrated model at this point. Nevertheless, $\mathrm{H_{AGN}}$ proves to be a very useful model that avoids several *ad-hoc* assumptions adopted in previous studies, and significantly improves the predictions of the non-sphericity of galaxy clusters. Also the quantitative comparison with $\mathrm{H_{noAGN}}$ and $\mathrm{H_{DM}}$ clarifies the impact of baryon physics on gas, star, and dark matter distribution.

2.2 Spherically-averaged profiles of density and temperature

Reliable modeling of XSB of galaxy clusters crucially depends on baryon physics that is incorporated in the simulations. In particular, it is widely known that AGN feedback plays an important role (e.g.,

Dubois et al. 2010, 2011). This is also clear from the comparison between $\mathrm{H_{AGN}}$ and $\mathrm{H_{noAGN}}$.

Figure 1 illustrates the density and temperature profiles of one simulated cluster ($M_{200} \approx 4.5 \times 10^{14} M_{\odot}$) in $\mathrm{H_{noAGN}}$. In the left-panel, we plot the density profiles of gas (red), dark matter (black), and stars (blue). Also, the (mass-weighted) gas temperature profile is shown in the right panel. Both the strong excess of the central stellar and gas densities and the sudden decrease of the central gas temperature are inconsistent with the typical profiles of observed galaxy clusters, and should be ascribed to the unrealistic over-cooling of gas in the region. This indicates that the feedback from SNe is not sufficient to stop star formation and gas-cooling in the central region.

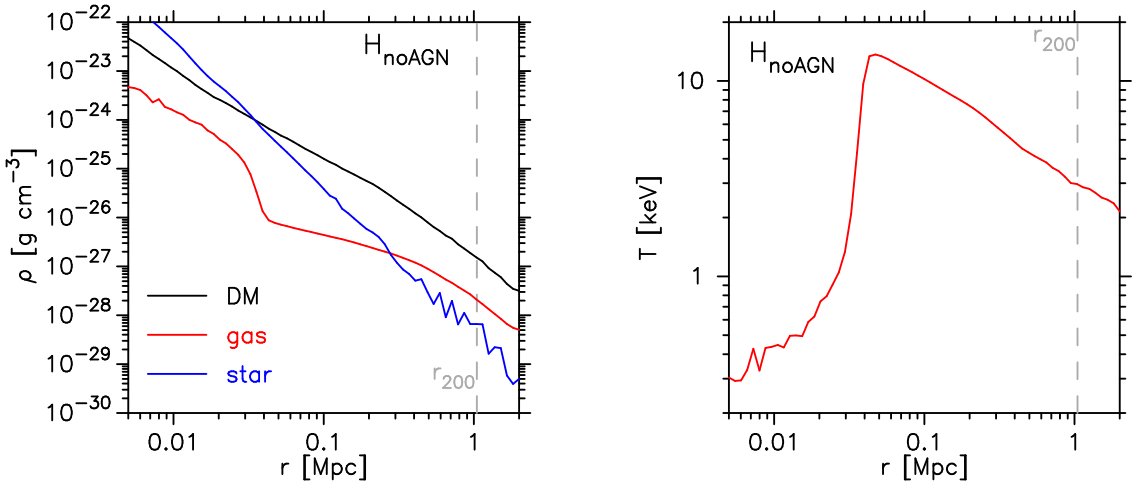

Fig. 1. Radial profiles of density (left) and mass-weighted gas temperature (right) of the cluster with $M_{200} \sim 4.5 \times 10^{14} M_{\odot}$ for $\mathrm{H_{noAGN}}$. The density profiles of gas (red), dark matter (black), and stars (blue) are shown in the left panel. The gray dashed vertical line indicates r_{200} of the cluster.

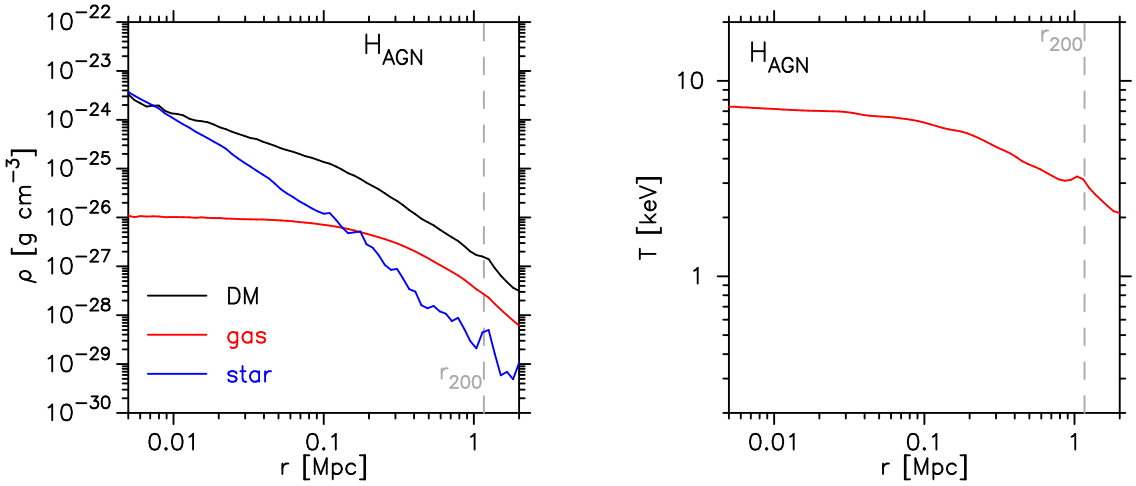

Fig. 2. Same as Figure 1, but for the corresponding cluster in $\mathrm{H_{AGN}}$. Note that r_{200} is slightly different between $\mathrm{H_{AGN}}$ and $\mathrm{H_{noAGN}}$.

In contrast, the corresponding cluster in $\mathrm{H_{AGN}}$ exhibits density and temperature profiles that are consistent with observed non-cool core clusters (see Figure 2; and also Okabe and Smith 2016;

Snowden et al. 2008). The stellar density exceeds the dark matter density inside $\sim$ 10 kpc, corresponding to the typical galactic scale. The gas density profile is flat inside $\sim$ 100 kpc, and does not exhibit a rapid increase unlike in Figure 1. Also, the gas temperature gradually increases toward the center, and the temperature at around $r \lesssim 0.5 r_{200}$ is consistent with the observed mass-temperature relation (Arnaud & Evrard 1999).

2.3 Estimate of non-sphericity

We use the mass tensor to estimate the non-sphericity of dark matter density distribution:

$$I_{\alpha\beta} = \sum_{i}^{N} m^{(i)} x_{\alpha}^{(i)} x_{\beta}^{(i)} \qquad (\alpha, \beta = 1, 2), \tag{2}$$

where $m^{(i)}$ and $x_{\alpha}^{(i)}$ are the mass and the projected position vector of the i-th particle within a given enclosed mass region (specified by the value of N). The mass tensor is computed iteratively until it is converged following Suto et al. (2016b), yielding the semi-minor axis a_1 and semi-major axis a_2 for projected ellipses. In what follows, we denote the projected axis ratio by $q \equiv a_1/a_2 (< 1)$.

For each of 40 simulated clusters, we calculate the projected dark matter density distribution along the x-, y-, and z-axes and determine the ellipses by using the mass tensor $I_{\alpha\beta}$. In later sections, we show the axis ratio q of XSB with a fixed value of a_2; $a_2/r_{200} = 0.1$, 0.2,..., 0.9, and 1.0. Hence we attempt to derive q from the dark matter component using the same values of a_2/r_{200}, in order to make a direct comparison and with that from S_X. $I_{\alpha\beta}$ is, however, defined for a fixed value of the enclosed mass, while the corresponding value of a_2 is not known in advance. We thus determine the axis ratios iteratively until the resultant value a_2 is converged within one percent. The same procedure is repeated for dark matter particles in $\mathrm{H_{DM}}$, $\mathrm{H_{noAGN}}$, and $\mathrm{H_{AGN}}$. The non-sphericity of stellar mass density distribution in $\mathrm{H_{noAGN}}$ and $\mathrm{H_{AGN}}$ is also estimated in the same fashion.

The mass tensor defined by equation (2) cannot be directly used to estimate the non-sphericity of XSB that is defined on grids, instead of particles. Thus we first compute

$$S_X(\vec{\theta}) = \frac{1}{4\pi(1+z)^4} \int dl\, n_{\mathrm{gas}}^2 \Lambda(T, Z) \tag{3}$$

along the line-of-sight within a sphere of r_{200} around each cluster center, where $n_{\mathrm{gas}} = n_{\mathrm{gas}}(\vec{\theta}, l)$ is the number density of gas and $\Lambda(T, Z)$ is the X-ray cooling function that depends on the gas temperature $T(\vec{\theta}, l)$ and metallicity $Z(\vec{\theta}, l)$. Note that, over the typical temperature range of galaxy clusters (1 keV $\lesssim T \lesssim$ 10 keV), $\Lambda(T, Z)$ is approximately proportional to $T^{1/2}$, and therefore the shape of S_X is largely determined by the gas density.

For each cluster, we calculate S_X projected along the x-, y-, and z axes according to Equation (3). We use the package `SPEX` to calculate the cooling function $\Lambda(T, Z)$ for the photon energy band

of $0.5\mathrm{keV} < E < 10\mathrm{keV}$.

In computing S_X, earlier SPH simulations had to exclude the contribution from cold and dense gas particles because this may overestimate the density of nearby hot X-ray emitting particles (Croft et al. 2001; Kay et al. 2002). This can be a serious issue especially for low resolution simulations in which the different gas phases are not well resolved. We believe that this is not a problem for our present simulations because the gas densities are properly estimated on individual cells, and also the mass and spatial resolutions are significantly improved than those in their SPH simulations.

Then we directly fit ellipses to $S_X(\vec{\theta})$. We adopt the fitting procedure of Jedrzejewski (1987) following Kawahara (2010). For each simulated cluster, we identify the ellipses with semi-major axis a_2 fixed to $a_2/r_{200} = 0.1$, 0.2, 0.3, and 0.4. Then the number of free parameters in the fitting procedure is four; the axis ratio $q \equiv a_1/a_2$, direction of the major axis Θ and the central position $\boldsymbol{X}_c$ in the projected profile.

Figure 3 shows the distribution of S_X (top), dark matter density (middle) and stellar density (bottom), projected along z-axis for the same cluster plotted in Figure 1. The left and right panels correspond to $\mathrm{H_{noAGN}}$ and $\mathrm{H_{AGN}}$, respectively. The black curves illustrate the ellipses with the semi-major axis $a_2/r_{200} = 0.1$, 0.2, 0.3, and 0.4.

Comparing the ellipses for the three components in $\mathrm{H_{AGN}}$, S_X appears more spherical, but the stellar density distribution is more elongated, than the dark matter density distribution. The former is consistent with the expectation that the gas distribution follows the isopotential surfaces. We also note that the orientations of those ellipses are similar among the three components, but they are not necessarily concentric.

In contrast, the dark matter and stellar density distributions in $\mathrm{H_{noAGN}}$ are significantly more spherical than those in $\mathrm{H_{AGN}}$. This indicates that the baryonic processes have strong impacts on the non-sphericity of collisionless particles, even beyond the central regions of galaxy clusters (Debattista et al. 2008; Teyssier et al. 2011; Bryan et al. 2013; Butsky et al. 2015; Cui et al. 2016). In the next section, we examine in more detail the statistics and correlation of the projected axis ratios of the three components.

3 Statistics and correlation of the non-sphericity of gas, star, and dark matter distribution

3.1 Effect of baryonic physics on dark matter distribution

As shown in the previous section, the baryon physics affects the non-sphericity of dark matter distribution significantly, perhaps more than what we naively expect. We first examine this surprising result more quantitatively below.

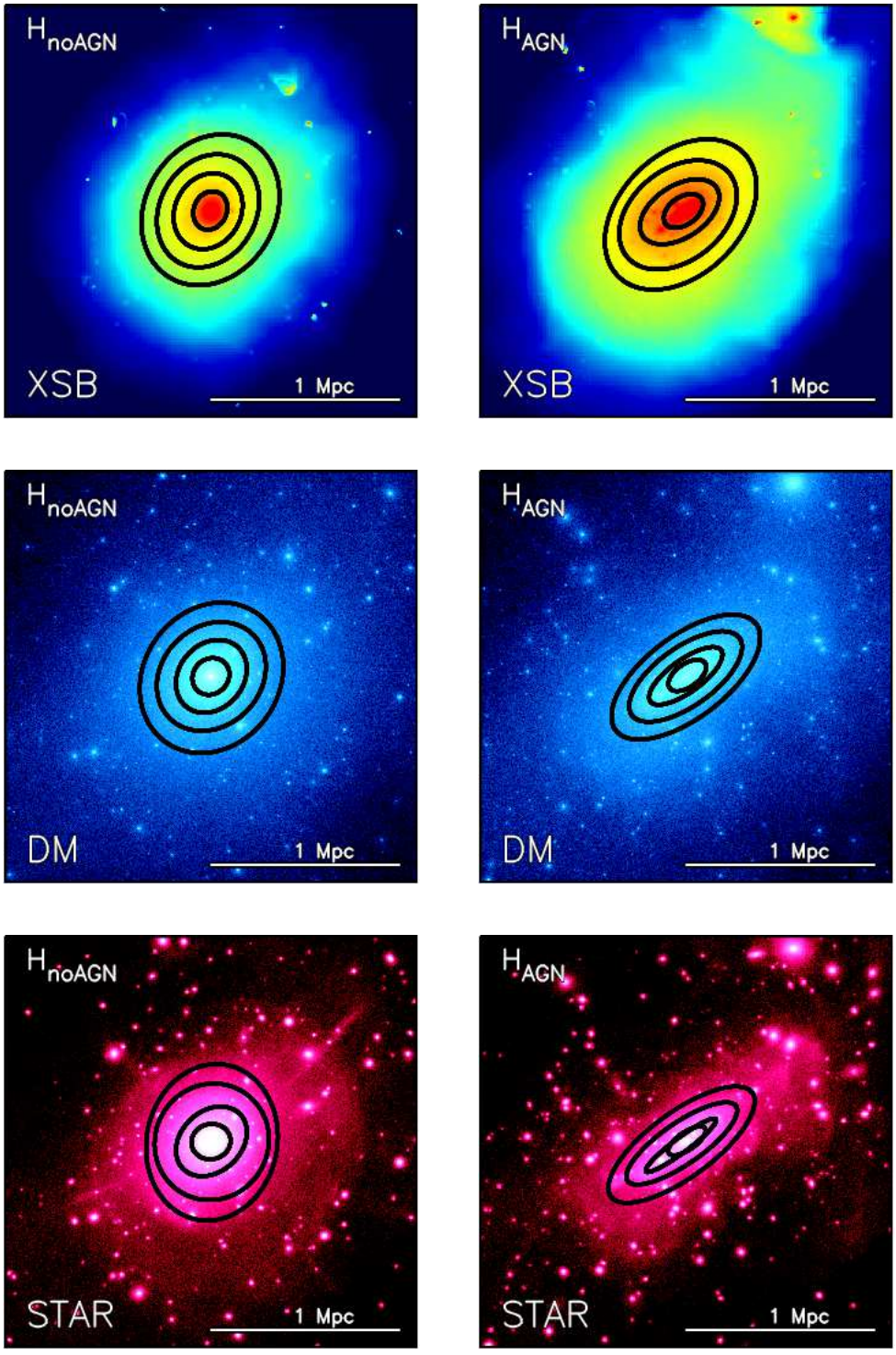

Fig. 3. X-ray surface brightness S_X (top), dark matter density distribution (middle), and stellar density distribution (bottom) of the same cluster plotted in Figure 1 projected along the z-axis; $\mathrm{H_{noAGN}}$ (left) and $\mathrm{H_{AGN}}$ (right). For each panel, the ellipses with the semi-major axis $a_2/r_{200} = 0.1$, 0.2, 0.3, and 0.4 are plotted in black curves. The ellipses are obtained by direct fitting for S_X, and by mass tensor for dark matter and stars.

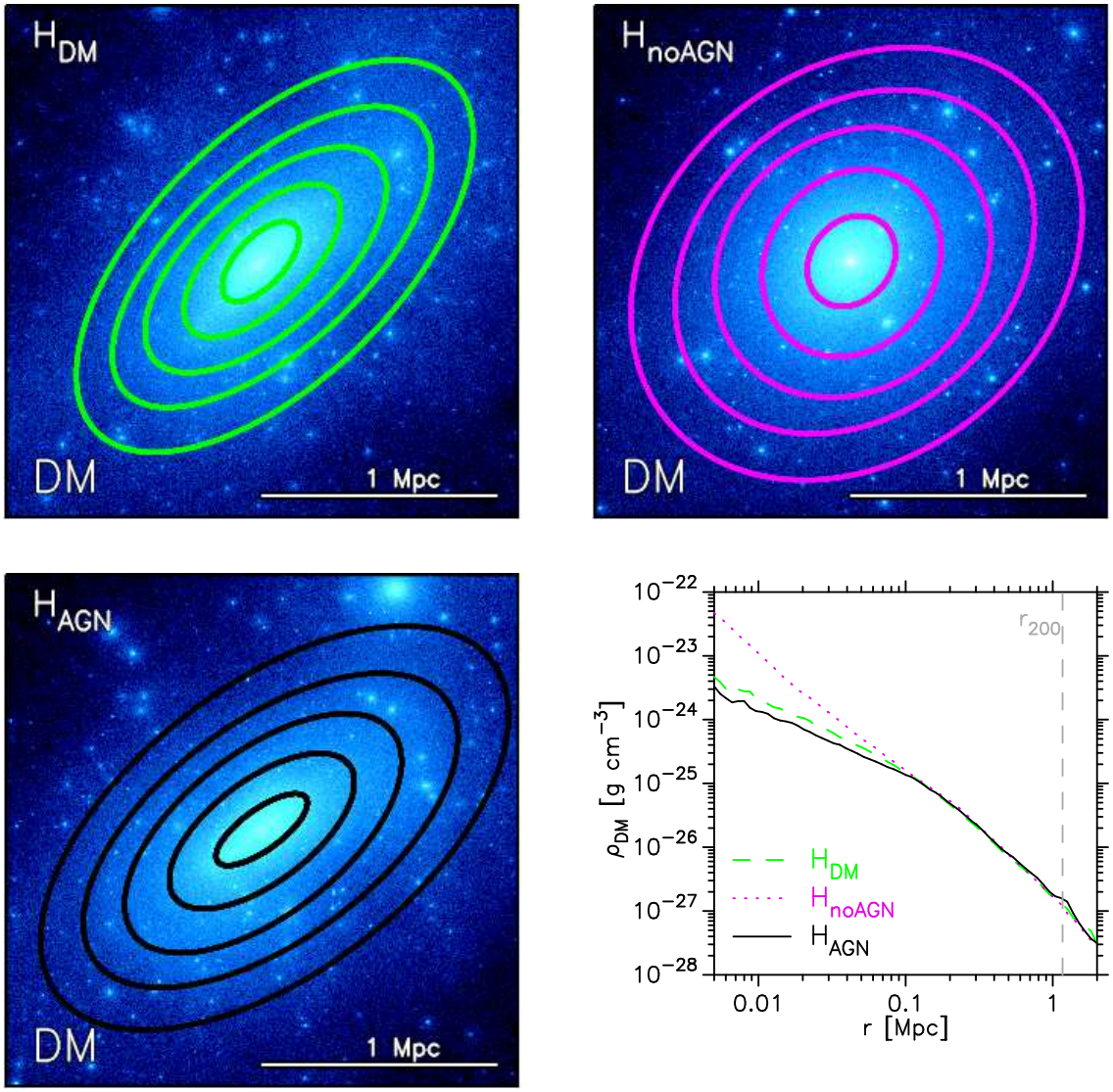

Fig. 4. Dark matter density distribution of the same cluster in Figure 1 projected along the z-axis of the simulation for three simulations; $\mathrm{H_{DM}}$ (upper-left), $\mathrm{H_{noAGN}}$ (upper-right) and $\mathrm{H_{AGN}}$ (lower-left). The fitted ellipses with the semi-major axis $a_2/r_{200} = 0.2$, 0.4, 0.6, 0.8, 1.0 are plotted in black curves. The corresponding dark matter density profiles are shown in the lower-right panel; $\mathrm{H_{DM}}$ (green), $\mathrm{H_{noAGN}}$ (magenta) and $\mathrm{H_{AGN}}$ (black). The dashed vertical line indicates r_{200} in $\mathrm{H_{AGN}}$. For $\mathrm{H_{DM}}$, the density profile is multiplied by a factor of $1 - \Omega_{b,0}/\Omega_{m,0} \approx 0.83$.

Figure 4 plots the projected dark matter distribution of the same cluster in Figures 1 and 2, extracted from $\mathrm{H_{DM}}$ (upper-left), $\mathrm{H_{noAGN}}$ (upper-right), and $\mathrm{H_{AGN}}$ (lower-left). The ellipses computed from the mass tensor corresponding to the semi-major axis of $a_2/r_{200} = 0.2$, 0.4, 0.6, 0.8, and 1.0 are plotted in solid curves. The lower-right panel shows the *spherically averaged* profiles of dark matter density for $\mathrm{H_{DM}}$ (green), $\mathrm{H_{noAGN}}$ (magenta) and $\mathrm{H_{AGN}}$ (black). Because the three runs adopt the same value for the matter density $\Omega_{m,0}$ and the run $\mathrm{H_{DM}}$ does not consider the baryon component, the dark matter mean density is different for this run; $\Omega_{\mathrm{CDM},0} = \Omega_{m,0}$ for $\mathrm{H_{DM}}$, but $\Omega_{\mathrm{CDM},0} = \Omega_{m,0} - \Omega_{b,0}$ for

$\mathrm{H_{AGN}}$ and $\mathrm{H_{noAGN}}$. Thus the density profile of $\mathrm{H_{DM}}$ in the lower-right panel is multiplied by a factor of $1 - \Omega_{b,0}/\Omega_{m,0} (\approx 0.83)$.

As is shown in the lower-right panel, the spherically averaged dark matter density profiles for $r > 0.1$Mpc are almost the same for the three runs. On the contrary, the inner profiles are significantly affected by baryon physics. The effect is particularly strong for $\mathrm{H_{noAGN}}$ that neglects the AGN feedback; the gas over-cooling pulls gas and stars towards the center, and then dark matter particles in the outer region fall into the central region. The AGN feedback, however, suppresses the gas over-cooling and flattens the inner density profile (Peirani et al. 2008; Dubois et al. 2010, 2011; Teyssier et al. 2011; Martizzi et al. 2013; Peirani et al. 2016). Thus the dark matter density profile of $\mathrm{H_{AGN}}$ turns out to be fairly close to the result for dark matter only simulation ($\mathrm{H_{DM}}$). Qualitatively speaking, the above tendency may be consistent with what we expect.

In order to make more quantitative comparison, we show in Figure 5 the projected axis ratios q for the 40 simulated clusters (viewed from three different line-of-sights) against their counterparts in $\mathrm{H_{DM}}$ at $a_2 = 0.2 r_{200}$ (*top*), $a_2 = 0.5 r_{200}$ (*middle*), and $a_2 = r_{200}$ (*bottom*). We note that $0.2 r_{200}$ and $0.5 r_{200}$ roughly correspond to the mass scales of M_{2500} and M_{500}.

Although the lower-right panel in Figure 4 may be interpreted that the baryonic effect is largely absent for $r > 0.1$Mpc, Figure 5 indicates that it is not the case as long as the non-sphericity is concerned. The dark matter distribution in $\mathrm{H_{noAGN}}$ is significantly rounder than, and not so correlated with, that in $\mathrm{H_{DM}}$. This result would be caused by the unrealistic gas over-cooling in the absence of AGN feedback. With the AGN feedback, $q_{\mathrm{DM}}(\mathrm{H_{AGN}})$ is roughly correlated with $q_{\mathrm{DM}}(\mathrm{H_{DM}})$ but with large scatters. The deviation between $q_{\mathrm{DM}}(\mathrm{H_{AGN}})$ and $q_{\mathrm{DM}}(\mathrm{H_{DM}})$ becomes weaker for outer regions, but still clearly exists even around the virial radius, $a_2 = r_{200}$. This implies that the baryon processes around the inner region of galaxy clusters affect the overall shape of their dark matter halos, which is indeed surprising.

To see statistically the effect of baryons on the non-sphericity of dark matter halos, we compute the probability density function (PDF) of the projected axis ratios. Figure 6 shows the result for $\mathrm{H_{DM}}$ (top), $\mathrm{H_{noAGN}}$ (middle), and $\mathrm{H_{AGN}}$ (bottom). To compensate for the small number of clusters, we plot the combined PDFs at $a_2/r_{200} = 0.1$, 0.2, 0.3, and 0.4 (left), 0.5, 0.6, and 0.7 (middle) and 0.8, 0.9, and 1.0 (right); the number of samples is 480, 360, and 360, respectively.

At the scale of $0.1 \leq a_2/r_{200} \leq 0.4$, the PDF of q_{DM} for $\mathrm{H_{DM}}$(top) is basically consistent with the result of Suto et al. (2016b) for M_{2500} ($r_{2500} \approx 0.2 r_{200}$), although the number of dark matter halos is much smaller due to the smaller box size of the Horizon simulation. The PDF of q_{DM} for $\mathrm{H_{noAGN}}$ (middle panel of Figure 6) is systematically shifted towards the right, relative to that of $\mathrm{H_{DM}}$; the dark matter density distribution is significantly rounder. If the AGN feedback is included (bottom), the

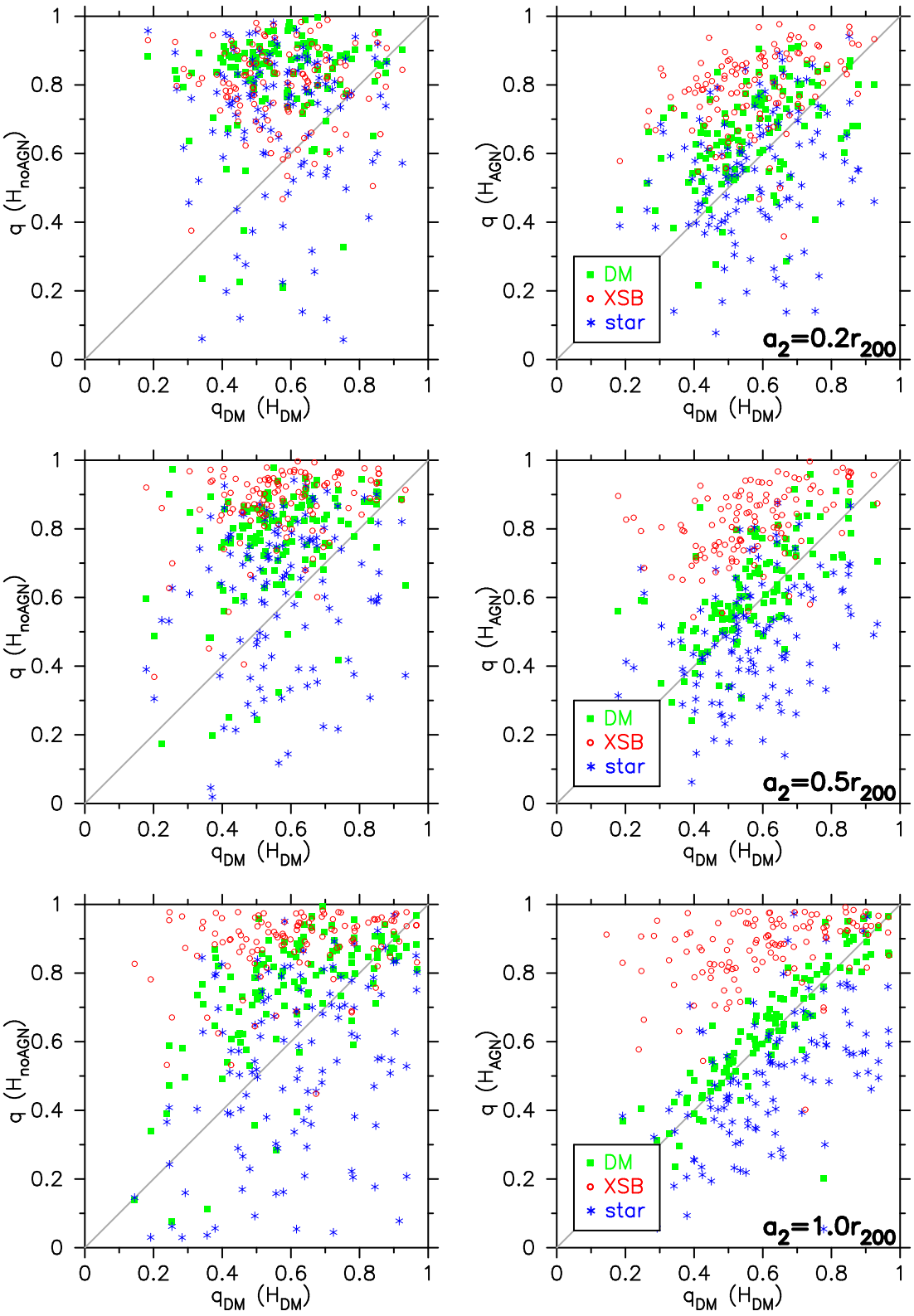

Fig. 5. Projected axis ratios of simulated clusters in $\mathrm{H_{AGN}}$ (*left*) and $\mathrm{H_{noAGN}}$ (*right*) against their counterparts in $\mathrm{H_{DM}}$; $a_2 = 0.2r_{200}$ (*upper*), $a_2 = 0.4r_{200}$ (*middle*), and $a_2 = r_{200}$ (*lower*).

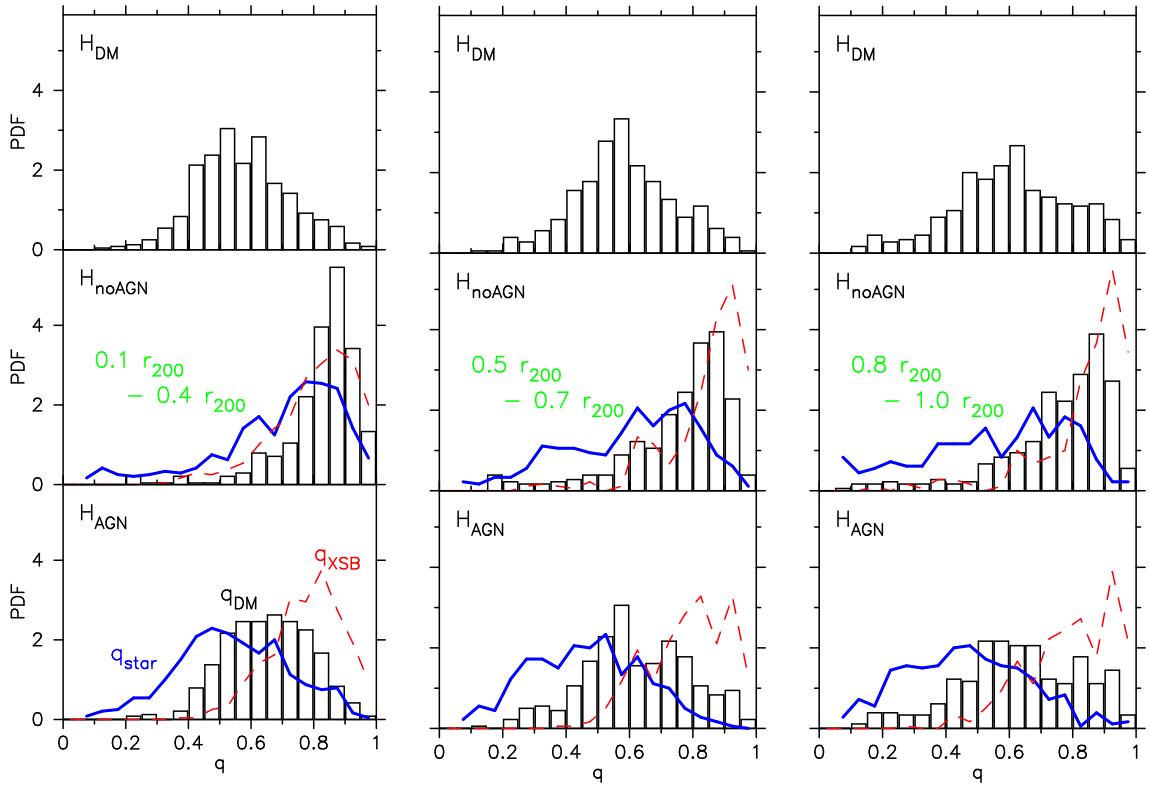

Fig. 6. PDFs of projected axis ratio of dark matter density distribution for the 40 simulated cluster along three lines-of-sight (x-, y-, and z-axes of the simulation). For each cluster, ellipses with the semi-major axis $a_2/r_{200} = 0.1$, 0.2,..., 0.9, and 1.0 are fitted by the mass tensor, and the PDF is calculated for the ellipses with $a_2 = 0.1$ - 0.4 r_{200} (left), 0.5 - 0.7 r_{200} (middle) and 0.8 - 1.0 r_{200} (right). The same analysis is performed for the three kinds of simulations; $\mathrm{H_{DM}}$ (top), $\mathrm{H_{noAGN}}$ (middle) and $\mathrm{H_{AGN}}$ (bottom). For $\mathrm{H_{AGN}}$ and $\mathrm{H_{noAGN}}$, the PDFs of the axis ratios of stellar density and XSB distributions are also plotted in blue solid and red dashed lines, respectively.

density distribution is only slightly rounder than that of $\mathrm{H_{DM}}$.

For reference, we plot the PDFs of $q_{\rm star}$ (blue solid lines) and $q_{\rm XSB}$ (red dashed lines) for $\mathrm{H_{noAGN}}$ and $\mathrm{H_{AGN}}$ in Figure 6. For both runs, the PDF of $q_{\rm star}$ is slightly shifted to the left (less spherical) compared to that of dark matter in each run. This is partly because the mass tensor, equation (2), is sensitive to substructures, i.e., galaxies at large radii. The PDFs of $q_{\rm star}$, $q_{\rm XSB}$, and $q_{\rm DM}$ for $\mathrm{H_{noAGN}}$ are all systematically shifted to the right, relative to those for $\mathrm{H_{AGN}}$ due to the over-cooling.

The PDFs in Figure 6 statistically confirm the visual impression of Figures 3 and 4, and indicate that the baryon processes around the central region have a strong impact on the shape of galaxy clusters represented by dark matter even at their virial radii. This is surprising given that the spherically-averaged density profiles are roughly the same among the three runs, and that the dark matter occupies a much larger mass fraction ($\approx$ 80 %) than gas and stars.

Kazantzidis et al. (2004) showed that dark matter halos in a simulation without radiative gas cooling are much less spherical than those in a simulation with cooling (both simulations do not in-

clude AGN feedback) up to the virial radius ($\approx r_{200}$). Their result also indicates that the shape of dark matter halos is strongly influenced by the detail of baryonic processes implemented in simulations. (Note that, since they adopted a definition of mass tensor somewhat different from equation (2), their results should not be quantitatively compared with ours.) We admit that the reason why the baryon physics influences the shape of the outer region of dark matter halo is not yet fully explained, and would like to defer the problem to the future study.

The above results indicate that dark matter alone simulations cannot be used even to predict the non-sphericity of dark matter distribution.

3.2 Mass- and Radial-Dependence of the axis ratio

Next we consider the mass dependence of the axis ratio q of SXB of simulated galaxy clusters. Figure 7 plots $q_{\rm XSB}$ at $a_2 = 0.4r_{200}$ for each simulated cluster along three lines-of-sight against its M_{200} for $\rm H_{AGN}$ (left) and $\rm H_{noAGN}$ (right). For each cluster, the measured $q_{\rm XSB}$ along the x-, y-, and z-axis are plotted in red squares, green triangles, and blue circles, respectively. Even for the same cluster, q can be quite different depending on the lines-of-sight; for example, if a cluster is elongated along the z-axis, q for the projection along x- or y-axis is much smaller than that along the z-axis.

We divide the 40 clusters into four groups of 10 clusters in the decreasing order of M_{200}. The mean value of $q_{\rm XSB}$ and the standard deviation are indicated by the black circle with error-bar in Figure 7. The mean $q_{\rm XSB}$ in $\rm H_{noAGN}$ ($\sim$0.84) is slightly larger then that in $\rm H_{AGN}$ $\sim$0.78. This reflects the rounder shapes of the dark matter halos in $\rm H_{noAGN}$, but the difference of $q_{\rm XSB}$ between the two simulation runs is smaller than that of dark matter.

In Figure 7 we find that the mass dependence of $q_{\rm XSB}$ is very weak both in $\rm H_{noAGN}$ and $\rm H_{AGN}$, although their scatter is fairly large. We also find that $q_{\rm XSB}$ depends only weakly on the radius of galaxy clusters. This is illustrated in Figure 8, where the mean and standard deviation of $q_{\rm XSB}$, $q_{\rm star}$, and $q_{\rm DM}$ computed over all the simulated clusters are plotted against a_2/r_{200}; $\rm H_{noAGN}$ (left) and $\rm H_{AGN}$ (right).

The blue triangles in Figure 8 indicate that the density distribution of stars is less spherical than that of dark matter for both simulations. Also, the mean $q_{\rm star}$ is higher in $\rm H_{noAGN}$ than in $\rm H_{AGN}$, as in the case of dark matter. The mean $q_{\rm star}$ tends to be larger toward the center for both simulations. This may be partly interpreted as the effect of the cosmic web where more galaxies at outer regions are accreted preferentially along the filaments (Aubert et al. 2004; Welker et al. 2015).

Consider first $\rm H_{noAGN}$. In the innermost region ($a_2 = 0.1r_{200}$), dark matter distribution is more spherical than that of XSB and stars. Since the gravitational potential there is dominated by stars (left

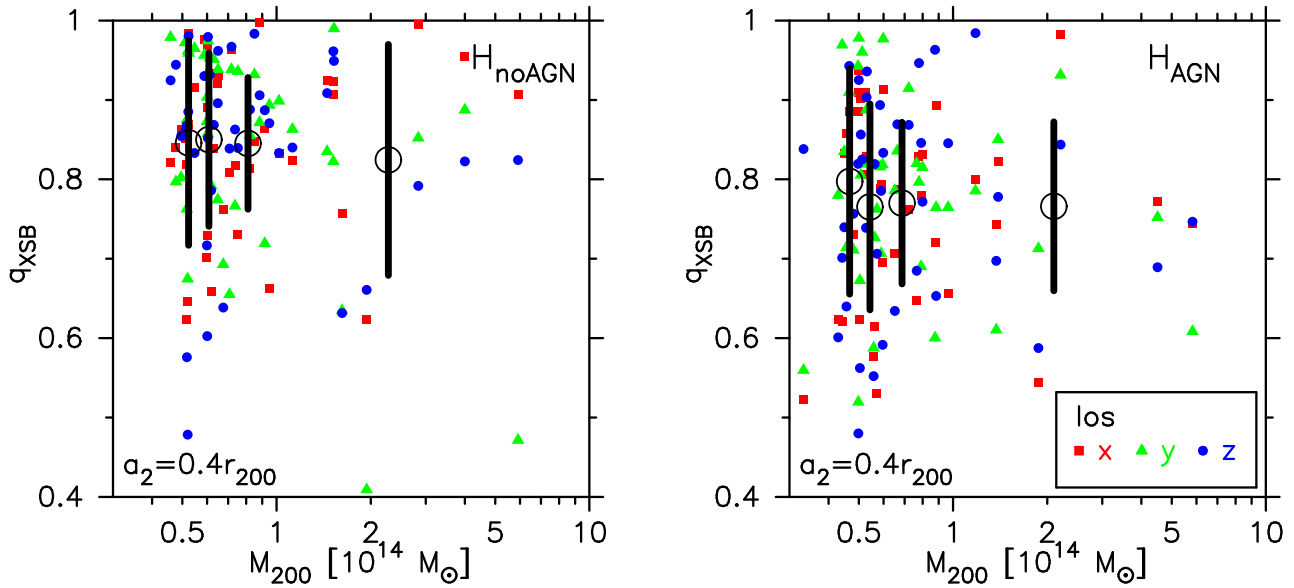

Fig. 7. Projected axis ratio q of the X-ray surface brightness with $a_2 = 0.4r_{200}$, against M_{200} of each simulated cluster, for $\mathrm{H_{noAGN}}$ (left) and $\mathrm{H_{AGN}}$ (right). Each symbol indicates the result for a simulated cluster. The axis ratio q of each cluster is measured along the three different lines-of-sight, and indicated in different symbols; x-axis (red square), y-axis (green triangle), z-axis (blue circle). The black circles show the averaged values of q over every 10 of 40 clusters, and the black lines indicate the corresponding standard deviation.

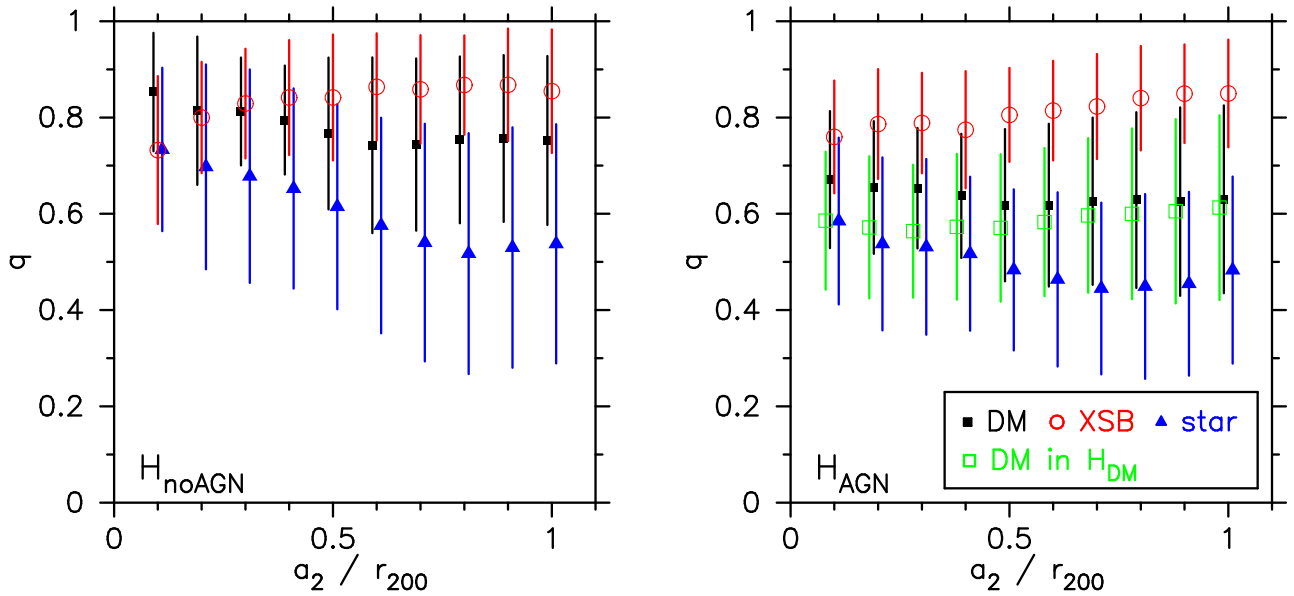

Fig. 8. Projected axis ratio q of the X-ray surface brightness (red), dark matter (black), and stars (blue) for the semi-major axis $a_2/r_{200} = 0.1$, 0.2, $\cdots$ 0.9, and 1.0, averaged over the 40×3 clusters, for $\mathrm{H_{noAGN}}$ (left) and $\mathrm{H_{AGN}}$ (right). The lines indicate the standard deviation. To facilitate visualization, the results for dark matter and stars are slightly shifted to the left and right, respectively.

panel of Figure 1), $q_{\rm XSB}$ is expected to be larger than $q_{\rm star}$ if the HSE assumption holds. Therefore Figure 8 implies that gas in $\rm H_{noAGN}$ is not in HSE in the innermost region. This is most likely simply due to the unrealistic over-cooling of gas in $\rm H_{noAGN}$, and indicates that the baryon physics needs to be properly incorporated in simulations in order to predict the non-sphericity of central regions of galaxy clusters.

Next we examine $\rm H_{AGN}$ in detail. As shown in the right panel of Figure 8, the mean value of $q_{\rm XSB}$ is roughly 0.8 and very weakly increases from inner to outer regions. In contrast, both $q_{\rm DM}$ and $q_{\rm star}$ decrease towards $a_2 \approx 0.5r_{200}$, and then become almost constant beyond the scale. For reference, we plot $q_{\rm DM}$ for $\rm H_{DM}$ in green open squares. While the mean values of $q_{\rm DM}$ in $\rm H_{DM}$ and $\rm H_{AGN}$ are almost the same for $a_2 > 0.5r_{200}$, $q_{\rm DM}$ in $\rm H_{DM}$ is significantly smaller for $a_2 < 0.5r_{200}$. Again this illustrates that the non-sphericity of galaxy clusters is significantly influenced, even up to the half of their virial radius, by the baryon physics operating around the more central regions. In other words, reliable predictions for the non-sphericity of dark matter inside $0.5r_{200}$, approximately corresponding to the mass scale of M_{500}, cannot be made with dark matter only simulations, and require the hydrodynamical simulations with well calibrated cooling and feedback effects.

4 Statistical comparison of the projected axis ratio of X-ray surface brightness of simulated and observed galaxy clusters

We finally calculate the PDF of $q_{\rm XSB}$ of our simulated clusters, and compare it with the data analyzed by Kawahara (2010). His sample of clusters is based on the XMM-Newton cluster catalog compiled by Snowden et al. (2008). Their selection of the sample is fairly empirical, but basically covers all clusters that permit the measurement of the temperature profile. Kawahara (2010) attempted the ellipse fit to all the 70 clusters in the catalog, and retained 61 clusters with the signal-to-noise ratio exceeding unity at $a_2 = 0.1r_{200}$ in constructing the PDF of the axis ratio. Also, he considers the axis ratio from 61, 56, 39 and 13 clusters at $a_2/r_{200} = 0.1, 0.2, 0.3$ and 0.4, respectively. This makes the total number of available measurements 169.

Since we have seen that $q_{\rm XSB}$ is fairly insensitive to radius and mass in the previous section, we combine the results for all the four semi-major axis lengths $a_2/r_{200} = 0.1$, 0.2, 0.3, and 0.4. The range of a_2/r_{200} is identical to that of Kawahara (2010). The resulting PDF is plotted in Figure 9. The number of the cluster sample is 480 (40 halos $\times$ 3 lines-of-sight $\times$ 4 semi-major axis lengths) for each simulation, but strictly speaking they are not necessarily independent.

In Figure 9, the histogram corresponds to the PDF of $q_{\rm XSB}$ for our simulated clusters. For comparison, the PDF of $q_{\rm DM}$ is over-plotted in green dashed line. Since the gas is supposed to trace

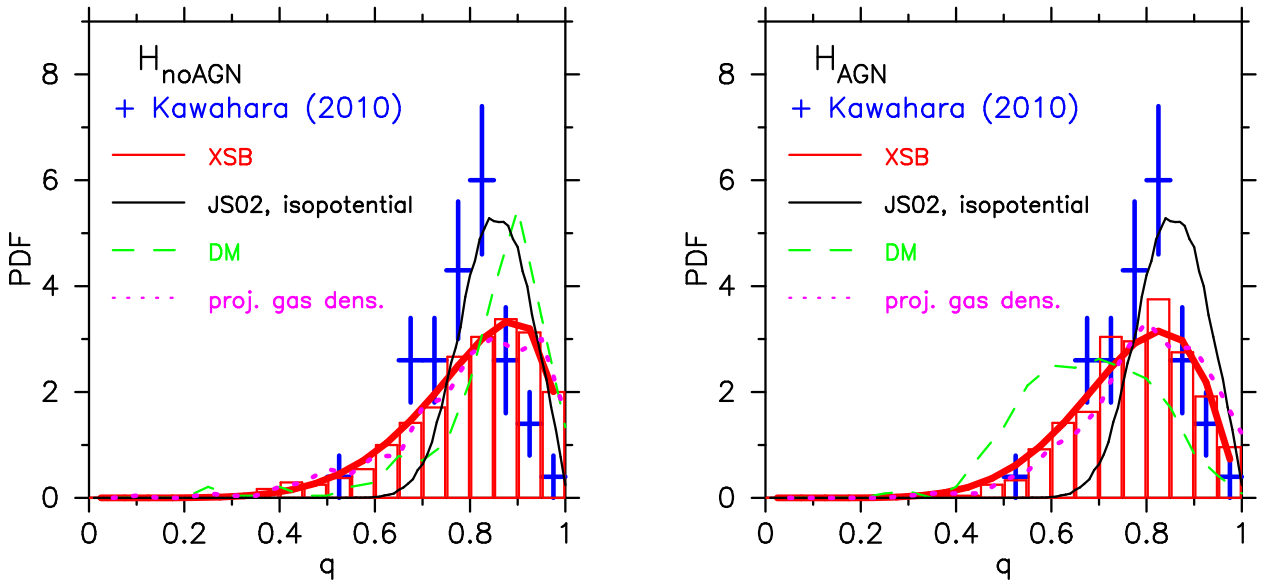

Fig. 9. PDFs of the projected axis ratio q; $\mathrm{H_{noAGN}}$ (left) and $\mathrm{H_{AGN}}$ (right). Results from numerical simulations are plotted for S_X in red histograms (fits to the β distribution are plotted in red thick lines), for dark matter in green dashed lines, and for gas in magenta dotted lines. The blue crosses with error-bars indicate the observational data compiled by Kawahara (2010). For comparison, the predictions based on the projected isopotential surfaces of self-similar triaxial dark matter profiles (Jing & Suto 2002; Lee & Suto 2003; Oguri et al. 2003) are shown in black solid lines.

the isopotential, instead of isodensity, surface of the total matter if HSE holds, their difference is qualitatively well understood. We also note that the PDF of $q_{\rm gas}$ for the projected gas density (magenta dotted lines) directly calculated from the simulation is roughly the same as the PDF of $q_{\rm XSB}$; while the projected gas density is proportional to $n_{\rm gas}$ and S_X is proportional to $n_{\rm gas}^2$, their shapes turn out to be roughly the same.

As in Suto et al. (2016b), we find that the histogram of projected axis ratio is reasonably well approximated by the beta distribution:

$$P(x;a,b) = \frac{x^{a-1}(1-x)^{b-1}}{B(a,b)}, \tag{4}$$

where

$$B(a,b) = \int_0^1 x^{a-1}(1-x)^{b-1}dx \tag{5}$$

is the beta function and a and b are the two fitting parameters. Their best-fit values for the PDF of $q_{\rm XSB}$ are $(a,b) = (6.74, 1.70)$ for $\mathrm{H_{noAGN}}$ and $(a,b) = (7.50, 2.31)$ for $\mathrm{H_{AGN}}$, which are over-plotted in thick red lines in Figure 9.

We also plot by the black solid curve the PDF of q for isopotential surfaces based on the PDF of $q_{\rm DM}$ modeled by JS02 assuming self-similar triaxial ellipsoids. As was shown in Suto et al. (2016b), the self-similar assumption of dark matter halos is not so accurate. Therefore, the difference between the black solid curves and the green dashed lines is explained by the combination of the break-down

of the self-similar assumption in JS02 and the baryon effects. The above result implies that the quantitative comparison with observations requires the direct analysis of numerical simulations with appropriate baryon physics as we performed here.

Kawahara (2010) derived the PDF of $q_{\rm XSB}$ from the observed 61 XMM-Newton clusters (plotted as blue crosses in Figure 9), and attempted a preliminary comparison with the PDF for isopotential surfaces (black solid curve) based on the model of JS02. We can perform more quantitative comparison using the prediction based on our hydrodynamical simulation (red histogram).

For that purpose, we use the cumulative PDF and apply the Kolmogorov-Smirnov (KS) test in order to avoid the binning effect due to the limited number of data. In general, the KS test is defined as follows. We consider an empirical distribution function $F_n(x)$, which is a cumulative distribution of n samples of x. Then we consider a null hypothesis that "$F_n(x)$ is drawn from $F(x)$" for any given cumulative distribution function $F(x)$. Then the KS statistic D_n is defined by

$$D_n = \sup_x |F(x) - F_n(x)|. \tag{6}$$

It is known that the quantity $\sqrt{n}D_n$ obeys the following distribution independently of $F(x)$ and $F_n(x)$:

$$p(\sqrt{n}D_n \leq x) = 1 - 2\sum_{i=1}^{\infty}(-1)^{i-1}e^{-2i^2x^2}. \tag{7}$$

In addition, for a confidence level α, K_α is defined by $p(\sqrt{n}D_n \leq K_\alpha) = 1-\alpha$. Then, if $\sqrt{n}D_n > K_\alpha$, the null hypothesis is rejected for the confidence level α.

First we consider the observational data analyzed by Kawahara (2010) and the prediction based on the isopotential surfaces of JS02 model as $F_n(x)$ and $F(x)$, respectively ($x = q$ and $n = 169$). Figure 10 shows the cumulative PDFs of the observation data (thin blue solid) and the PDF of q for the isopotential surfaces (black dashed). Note that the two panels show the results based on $\rm H_{noAGN}$ (left) and $\rm H_{AGN}$ (right), but these two lines (blue and black) are independent of simulations and thus the same for both panels. For these cumulative PDFs, we obtain $\sqrt{n}D_n = 3.89$, and the corresponding α is less than 10^{-7}. Hence the PDF of q for the isopotential surfaces is highly inconsistent with the observation data.

We next compare the observation data with our simulation results. In this case, both distributions are constructed from finite samples, thus we consider a modification to the KS statistic (6). For two empirical distribution functions, $F_n(x)$ and $G_m(x)$ respectively with n and m samples, the KS statistic can be generalized as

$$\bar{D}_{n,m} = \sup_x |F_n(x) - G_m(x)|. \tag{8}$$

Then the quantity $\sqrt{nm/(n+m)}\bar{D}_{n,m}$ follows the same PDF as Equation (7).

In this case, we regard the distribution of q for S_X of our simulated clusters as $G_m(x)$

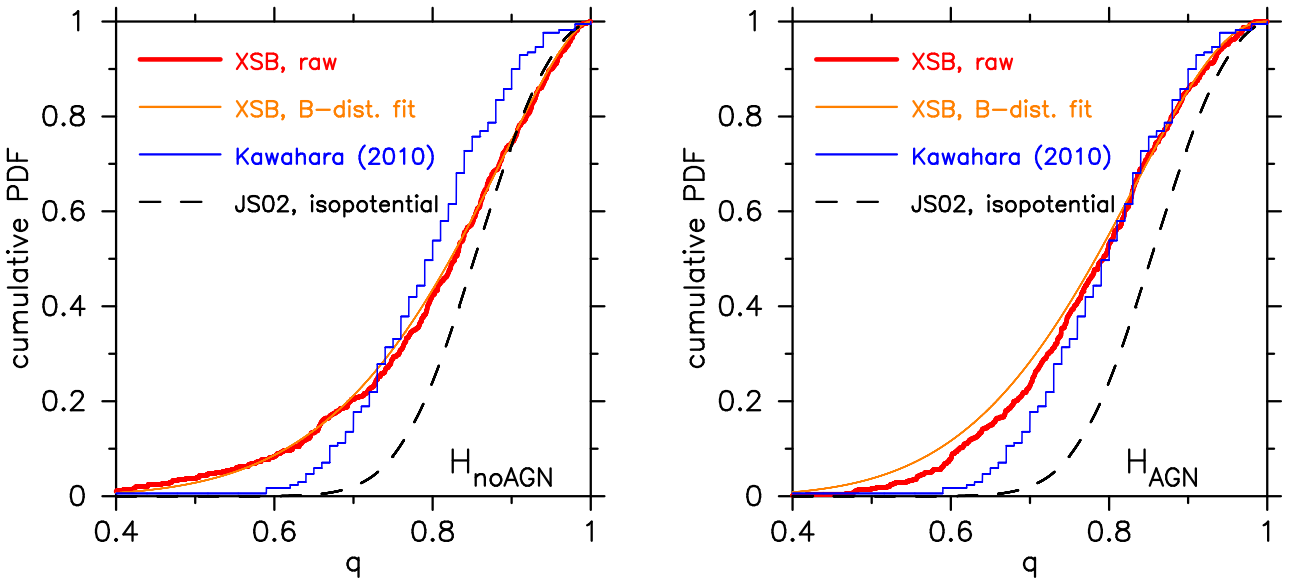

Fig. 10. Cumulative PDFs of q of the X-ray surface brightness S_X; $\mathrm{H_{noAGN}}$ (left) and $\mathrm{H_{AGN}}$ (right). Results from numerical simulations are plotted in thick red lines, and the corresponding fits on the basis of β distribution are plotted in thin orange lines against the observational data in blue histograms compiled by Kawahara (2010). For comparison, the predictions based on the projected isopotential surfaces of self-similar triaxial dark matter profiles (Jing & Suto 2002; Lee & Suto 2003; Oguri et al. 2003) are shown in black dashed lines.

($x = q$ and $m = 480$). The cumulative fraction for $q_{\rm XSB}$ is shown in thick red line in Figure 10 for $\mathrm{H_{noAGN}}$ (left) and $\mathrm{H_{AGN}}$. For $\mathrm{H_{noAGN}}$, we obtain $\sqrt{nm/(n+m)}\bar{D}_{n,m} = 2.04$, and the corresponding α is less than 10^{-3}. On the other hand, for $\mathrm{H_{AGN}}$, $\sqrt{nm/(n+m)}\bar{D}_{n,m} = 1.24$, and the corresponding α is 0.10. In other words, the probability that the observational data are drawn from the same distribution as our simulation results is 10 % for $\mathrm{H_{AGN}}$, and less than 0.1 % for $\mathrm{H_{noAGN}}$.

The agreement of our $\mathrm{H_{AGN}}$ result against the observation is not perfect, but much better than that of the previous prediction based on the various inaccurate assumptions (Lee & Suto 2003; Oguri et al. 2003; Kawahara 2010; Suto et al. 2016b). Thus we interpret this as promising and encouraging even though it is premature to put any further conclusion at this point. Instead we would like to note that there still remain several issues that need to be carefully examined in both observations and simulations. The statistical significance of the present result is limited by the available number of observed clusters with high-quality imaging data. In particlar, the observational data have much more weights at 0.1 and 0.2 a_2/r_{200}, while simulation data have the same weight. Also the mass ranges of the halos do not exactly match between observations and simulations, although the mass dependence is not so strong. Such biases need to be taken into account carefully. The systematic uncertainty of the predictions is dominated by the reliable implementation of baryon physics. Those issues will be improved with on-going and up-coming observational survey projects, and we plan to carry out systematic numerical simulations in order to address the reliability of the baryon physics modeling.

We hope to report the progress elsewhere in due course.

5 Summary and Conclusion

We have examined the non-sphericity of galaxy clusters using the projected axis ratios of X-ray surface brightness, star, and dark matter distributions ($q_{\rm XSB}$, $q_{\rm star}$, and $q_{\rm DM}$). We have extracted 40 clusters of mass larger than $3\times10^{13}M_\odot$ from cosmological hydrodynamic simulations that fully incorporate baryon physics.

In general, we find $q_{\rm XSB} > q_{\rm DM}$, which is qualitatively understood by the fact that the gas roughly traces the isopotential, instead of isodensity, surface of the total matter. Also our simulation indicates that $q_{\rm DM} > q_{\rm star}$, but this should be fairly sensitive to the baryon physics incorporated in the simulation. Indeed, the baryon physics, in particular the AGN feedback, has a significant impact on the non-sphericity of galaxy clusters. In terms of the spherically averaged *dark matter* profile, the baryon physics is important only in the region less than $\sim 10\%$ of the virial radius of each clusters. Nevertheless, its non-sphericity is affected even up to the half of the virial radius. For instance, the dark matter distribution becomes more spherical due to the baryon effect relative to the dark matter only simulations. Also the trend of increasing ellipticity of dark matter distribution against the radius is opposite to that predicted from simulations neglecting baryon physics. Only beyond the half of the virial radius, the non-sphericity of dark matter distribution is not much affected by the baryon physics operating in the central region. This should be kept in mind even when weak-lensing analysis is used in order to measure the non-sphericity of dark matter halos (Oguri et al. 2010; Suto et al. 2016b).

Then we have measured the projected axis ratio of X-ray surface brightness, $q_{\rm XSB}$, for the 40 simulated clusters, and obtained its probability density function. The latter is very different from the previous prediction based on the projected isopotential surfaces of self-similar triaxial dark matter profiles (Jing & Suto 2002; Lee & Suto 2003; Oguri et al. 2003), indicating the importance of the direct estimate from the numerical simulations. Therefore our resulting PDF significantly improves the reliability of the prediction, which should be useful in future observational confrontation.

Indeed while the previous prediction was not consistent with the observational data compiled by Kawahara (2010), our current improved prediction based on the hydro-simulation with the AGN feedback exhibits much better agreement. This is interesting and promising, but we admit that it is not yet fully satisfactory: the statistics is severely limited by the available number of high-quality clusters in both observations and in simulations. Furthermore the parameter dependence of the simulation, including cosmological parameters and empirical parameters that control the baryon processes, needs to be examined quantitatively.

Nevertheless our current study clearly indicates that the non-sphericity of galaxy clusters will serve as a useful quantitative probe of cosmology and cluster physics. The current methodology can be easily applied to the cluster sample from the Sunyaev-Zel'dovich survey, e.g., Kitayama (2014, 2016), and also in principle to weak-lensing (Oguri et al. 2003, 2010; Suto et al. 2016b). The joint analysis of X-ray surface brightness, the Sunyaev-Zel'dovich effect, and weak-lensing in an individual and/or statistical manner will provide an even more powerful approach to identify the nature of non-sphericity of galaxy clusters. Future observational data and simulations will be able to test the cold dark matter scenario and baryon physics simultaneously through the non-sphericity of galaxy clusters in a complementary fashion to the conventional statistics based on spherically averaged quantities.

Acknowledgements

We thank Hajime Kawahara and Masamune Oguri for useful discussions. The present work is based on the Horizon simulation runs, which have been performed using the HPC resources of CINES under the allocations 2013047012, 2014047012 and 2015047012 by GENCI. The post-processed analysis of the simulation was carried out on Cray XC30 at Center for Computational Astrophysics of National Astronomical Observatory of Japan, and also on the Horizon cluster at Institut d'Astrophysique de Paris. S.P. acknowledges support from the long-term invitation fellowship by Japan Society for the Promotion of Science (JSPS). This work is supported partly by JSPS Core-to-Core Program "International Network of Planetary Sciences", and by JSPS Grant-in-Aids for Scientific Research No. 26-11473 (D.S.), No. 25400236 (T.K.), and No. 24340035 (Y.S.).

References

Arnaud, M. & Evrard, A. E. 1999, MNRAS, 305, 631

Aubert, D., Pichon, C., & Colombi, S., 2004 MNRAS, 352, 376

Bryan, S. E., Kay, S. T., Duffy, A. R., Schaye, J., Dalla V. C., & Booth, C. M., 2013 MNRAS, 429, 3316

Butsky, I., Macciò, Andrea V., Dutton, A.A., Wang, L., Stinson, G. S., Penzo, C., Kang, X., Keller, B. W., & Wadsley, J., 2015, arXiv:1503.04814

Croft, R. A. C., Di Matteo, T., Davé, R., Hernquist, L., Katz, N., Fardal, M. A., & Weinberg, D. H., 2001 ApJ, 557, 67.

Cui, W., Power, C., Knebe, A., et al. 2016, MNRAS, 458, 4052

Debattista, V.P., Moore, B., Quinn, T., Kazantzidis, S., Maas, R., Mayer, L., Read, J., & Stadel, J., 2008 ApJ, 681, 1076

Dubois, Y. & Teyssier, R. 2008, A& A, 477, 79

Dubois, Y., Devriendt, J., Slyz, A., & Teyssier, R. 2010, MNRAS, 409, 985

Dubois, Y., Devriendt, J., Teyssier, R. & Slyz, A. 2011, MNRAS, 417, 1853

Dubois, Y., Devriendt, J., Slyz, A., & Teyssier, R. 2012, MNRAS, 420, 2662

Dubois, Y., Pichon, C., Welker, C. et al. 2014, MNRAS, 444, 1453

Fang, T., Humphrey, P., & Buote, D. 2009, ApJ, 691, 1648

Greggio, L. & Renzini, A. 1983, A& A, 118, 217

Haardt, F. & Madau, P. 1996, ApJ, 461, 20

Jedrzejewski, R. I. 1987, MNRAS, 226, 747

Jing, Y. P., Suto, Y., 2002, ApJ, 574, 538 (JS02)

Kawahara, H., 2010, ApJ, 719, 1926

Kay, S. T., Pearce, F. R., Frenk, C.S., & Jenkins, A., 2002, MNRAS, 330, 113.

Kazantzidis, S., Kravtsov, A. V., Zentner, A. R., Allgood, B., Nagai, D., & Moore, B., 2004, ApJL, 611, L73

Kitayama, T. 2014, PTEP, 6, 06B11124

Kitayama, T., Ueda, S., Takakuwa, T., et al., 2016, PASJ, in press (arXiv:1607.08833)

Komatsu, E., Smith, K. M., Dunkley, J. et al., 2011, ApJS, 192, 18

Leitherer, C., Ortiz Otálvaro, P. A., Bresolin, F. et al., 2010, ApJS, 189, 309

Leitherer, C., Schaerer, D., Goldader, J. D. et al., 1999, ApJS, 123, 3

Lau, E. T., Kravtsov, A. V., & Nagai, D. 2009, ApJ, 705, 1129

Lau, E. T., Nagai, D., & Nelson, K. 2013, ApJ, 777, 151

Lee, J., & Suto, Y. 2003, ApJ, 585, 151

Martizzi, D., Teyssier, R., & Moore, B., 2013, MNRAS, 432, 1947

Navarro J. F., Frenk C. S., White S. D. M., 1996, ApJ, 462, 563

Navarro J. F., Frenk C. S., White S. D. M., 1997, ApJ, 490, 493

Oguri, M., Lee, J. & Suto, Y., 2003, ApJ, 599, 7

Oguri, M., Takada, M., Okabe, N., & Smith, G. P., 2010, MNRAS, 405, 2215

Okabe, N., & Smith, G. P., 2016, MNRAS, 461, 3794

Omma, H., Binney, J., Bryan, G., & Slyz, A. 2004, MNRAS, 348, 1105

Peirani, S., Kay, S., & Silk, J. 2008, A&A, 479, 123

Peirani, S., et al. 2016, in preparation

Press, W. H. & Schechter, P., 1974, ApJ, 187, 425

Prunet, S., Pichon, C., Aubert, D., Pogosyan, D., Teyssier, R., & Gottloeber, S. 2008, ApJS, 178, 179

Rasera, Y. & Teyssier, R. 2006, A& A, 445, 1,

Snowden, S. L., Mushotzky, R. F., Kuntz, K. D., & Davis, D. S. 2008, A& A, 478, 615

Sutherland, R. S. & Dopita, M. A. 1993, ApJS, 88, 253

Suto, D., Kawahara, H., Kitayama, T., Sasaki, S., Suto, Y., & Cen, R. 2013, ApJ, 767, 79

Suto, D., Kitayama, T., Osato, K., Sasaki, S. & Suto, Y., 2016a, PASJ, 68, 14

Suto, D., Kitayama, T., Nishimichi, T., Sasaki, S. & Suto, Y., 2016b, PASJ, in press

Teyssier, R., Moore, B., Mrizzi, D., Dubois, Y., & Mayer, L. 2011, MNRAS, 414, 195

Welker, C., Dubois, Y., Pichon, C., Devriendt, J., & Chisari, E. N., 2015, Eprint arXiv:1512.00400